

Accelerated Time Integrator for Multiple Time Scale Homogenization

Robert Crouch and Caglar Oskay*

Department of Civil and Environmental Engineering
Vanderbilt University
Nashville, TN 37235

Abstract

This manuscript presents an accelerated time domain homogenization methodology for prediction of material and structural failure under fatigue loading. The methodology is based on mathematical homogenization theory applied to the time domain. The method addresses the computational challenge associated with the scale disparity between the characteristic fatigue load period and the overall fatigue life. Cycle sensitive continuum damage mechanics modeling is used to describe the progressive damage accumulation under fatigue loading. The original initial boundary value problem is decomposed into coupled fast and slow time scale problems. A quasilinear approximation to the fast time scale problem is introduced to efficiently evaluate the response under a fatigue load cycle. The effect of the new time integrator on the thermodynamic consistency of the resulting system of discrete equations is demonstrated for a general class of continuum damage mechanics models. The proposed method is numerically verified based on a scalar damage model and a spatially multiscale damage model used for predicting fatigue life of composite materials. The proposed accelerated time integrator is shown to have reasonable accuracy and is orders of magnitude more computationally efficient when compared to previously proposed time homogenization methods.

KEY WORDS: multiscale; fatigue; homogenization; model reduction; composite materials

1 Introduction

Modeling and prediction of the progressive damage accumulation and failure of brittle and quasibrittle materials subjected to cyclic loading has been a significant challenge for the

*Corresponding author address: VU Station B#351831, 2301 Vanderbilt Place, Nashville, TN 37235.
Email: caglar.oskay@vanderbilt.edu

computational community for many decades. A trend towards widespread use of composite materials in a range of industries such as aerospace and automotive has increased the stakes of predicting the long term behavior and durability of such materials. For instance, a lack of fatigue modeling capability for polymer composite materials and structures has led to overly conservative design strategies to prevent the sudden and catastrophic failures foretold with few visible indications. Highly conservative design strategies in turn offset the benefits of the composite materials, limiting their potential to provide higher performance.

One of the main approaches to modeling the initiation and growth of diffuse and widespread damage observed in materials has been Continuum Damage Mechanics (CDM) [7, 24]. CDM has been shown to describe the behavior of composite materials, particularly under monotonic loading conditions [26]. In CDM, a set of internal state variables (denoted as damage variables) track the evolution of microcrack or microvoid densities as a function of the response fields (i.e., strain, stress, strain energy) and as a function of the field gradients. The inclusion of the field gradients is necessary to regularize the problem, which otherwise exhibits damage localization and mesh sensitivity [38]. The resulting system of equations is often highly nonlinear, regardless of the evaluation method that includes the classical assumed strain approach [35] or the more recent phase-field method [6].

Extending the CDM framework to model damage accumulation under cyclic loading presents a significant challenge. The main issue is the computational intractability associated with solving a highly nonlinear problem that includes a very large number of time steps required to resolve each load cycle in a structure's load trajectory. This intractability has been recently addressed using a number of approaches including the cycle jump method [7, 9, 32, 18], manifold-based multitemporal modeling [2, 36], wavelet transformation [8, 22], and the multiple time scale homogenization [29, 30]. The common idea in these computational approaches is to approximate the evolution of a structure using the response from a small number of resolved cycles within the load trajectory of the structure and interpolating the response evolution between the resolved cycles.

We adopt the multiple time scale computational homogenization approach in this study. Computational homogenization [16, 19, 37] (CH) is a multiscale modeling approach, which is derived based on the mathematical homogenization theory [3, 4]. CH with multiple spatial scales has been employed to idealize the failure behavior of many heterogeneous materials, including composites under monotonic loads [13]. One of the key benefits of CH is the prediction of macroscale failure directly from a multiplicity of microscale failure mechanisms [11, 31]. The idea of CH has also been applied to the time domain to predict the cyclic response [29, 30]. Under fatigue loading, a time scale disparity exists between the characteristic period of the cyclic load and the overall life of the structure. The multiple time scale homogenization method bears a resemblance to the cycle jump techniques previously

proposed in the context of continuum damage mechanics models, but provides a rigorous computational framework for evolution of fatigue damage accumulation and prediction of life. More recently, Crouch and Oskay [12] developed a space-time homogenization method to study the fatigue behavior of composite materials that accounted for the presence of multiple spatial scales to address the material heterogeneity and multiple time scales. The space-time homogenization leads to a series of four coupled nonlinear space-time problems compared to the two-coupled spatial problems in CH with multiple spatial scales. While the homogenization method has been applied successfully for life prediction of problem domains with small size (i.e., coupon scale), it remains computationally very costly for performing large size structural analysis - a class of problems to which fatigue modeling offers the greatest potential benefit.

In this manuscript, an accelerated time integration scheme is proposed for the multiple time scale homogenization method. The approach in this manuscript admits a field decomposition of the form: $u(t) = \tilde{u}(t) + u^m(t, \tau)$, in which the oscillatory and the smooth components of the response field are of the same order of magnitude. In this regard, the approach is more akin to the variational multiscale method or multiscale finite element method [21, 28, 15] than the asymptotic expansions, which admit decomposition of the form: $u(t) = \tilde{u}(t) + \eta u^m(t, \tau)$. The expansions employed in the manuscript for evolution equations, when combined with the almost periodicity operator, result in $O(1)$ terms only. The proposed scheme relies on a stepwise-linear approximation of microchronological (single-cycle) problems using the assumption that damage accumulation within a single cycle remains small. The two key novel contributions of this manuscript are: (1) Formulation and implementation of the accelerated multiple time scale homogenization method. The proposed method is capable of accelerating the multiple time scale evaluation of damage accumulation response compared to those homogenization approaches previously proposed; and (2) Demonstration of the thermodynamic consistency of damage models integrated using the multiple time scale homogenization methods, in general, and the proposed accelerated time integration scheme, in particular, for a large class of CDM models. The proposed approach is thoroughly verified for two different CDM models to demonstrate the generality of this approach.

The remainder of this manuscript is organized as follows: Section 2 describes a general formulation of the fatigue damage accumulation and life prediction problem in the context of CDM. In Section 3, the fundamentals of the multiple time scale modeling is described. Section 4 details the application of the multiple time scale modeling principles to the fatigue damage accumulation and life prediction problem, along with the conditions which lead to the accelerated time integrator. Section 5 describes the computational implementation of the proposed method and the thermodynamic consistency of the accelerated time integration algorithm. In Section 6, a series of numerical verification studies are provided to assess the

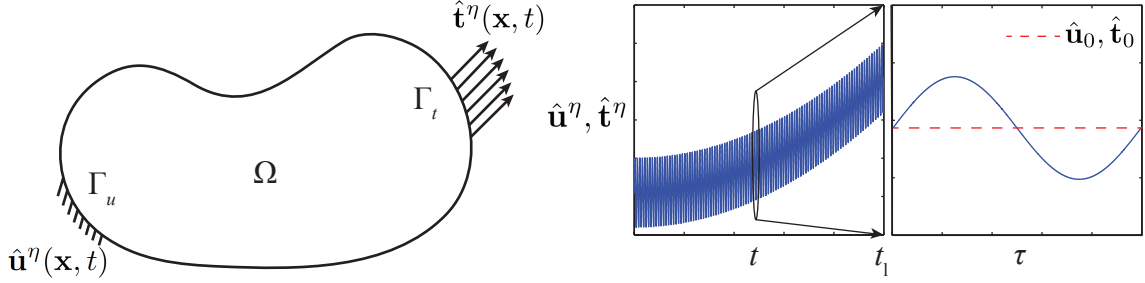


Figure 1: Schematic description of the problem domain subjected to fatigue loading.

performance and accuracy of the proposed method. Section 6 discusses the conclusions and future research in this area.

2 Problem formulation

Consider a body with its domain denoted as Ω subjected to a periodic and quasi-static excitation as illustrated in Fig. 1. \mathbf{x} denotes the spatial coordinate within Ω . Let $t \in [0, t_l]$ be the time coordinate, where t_l is the fatigue life of the body, taken as an unknown. The response of the body subjected to the periodic excitation is modeled using the following equilibrium equation:

$$\nabla \cdot \boldsymbol{\sigma}^\eta(\mathbf{x}, t) + \mathbf{b}(\mathbf{x}) = \mathbf{0}; \quad \mathbf{x} \in \Omega, \quad t \in [0, t_l] \quad (1)$$

where $\boldsymbol{\sigma}^\eta$ is the stress tensor, \mathbf{b} the body force per unit volume, and $\nabla \cdot (\cdot)$ the divergence operator. Fluctuation of the response fields in time due to the oscillatory (i.e. fatigue) loading is indicated by a superscript η . The loading rate is taken to be slow enough such that the inertial effects can be neglected.

Assuming small deformations, the strain tensor is expressed as the symmetric gradient of the displacement field:

$$\boldsymbol{\epsilon}^\eta(\mathbf{x}, t) = \nabla^s \mathbf{u}^\eta(\mathbf{x}, t) \quad (2)$$

where $\boldsymbol{\epsilon}^\eta$ is the strain tensor, \mathbf{u}^η the displacement field, and $\nabla^s(\cdot) = \frac{1}{2}[\nabla(\cdot) + (\cdot)\nabla]$ the symmetric gradient operator.

The fatigue loading is imparted on the body through the displacement and traction boundary conditions on $\Gamma_u \in \partial\Omega$ and $\Gamma_t \in \partial\Omega$ (such that $\Gamma_u \cup \Gamma_t = \partial\Omega$ and $\Gamma_u \cap \Gamma_t = \emptyset$), respectively, as:

$$\mathbf{u}^\eta(\mathbf{x}, t) = \hat{\mathbf{u}}^\eta(\mathbf{x}, t); \quad \mathbf{x} \in \Gamma_u, \quad t \in [0, t_l] \quad (3)$$

$$\boldsymbol{\sigma}^\eta(\mathbf{x}, t) \cdot \mathbf{n}(\mathbf{x}) = \hat{\mathbf{t}}^\eta(\mathbf{x}, t); \quad \mathbf{x} \in \Gamma_t, \quad t \in [0, t_l] \quad (4)$$

in which, $\hat{\mathbf{u}}^\eta$ and $\hat{\mathbf{t}}^\eta$ are prescribed boundary displacement and traction functions, taken to be oscillatory, and \mathbf{n} is the outward normal vector to the boundary of the body. For simplicity, the initial state of the body is taken to be stress and displacement free.

The constitutive relationship that describes the progressive accumulation of fatigue damage as a function of load cycles is modeled based on a thermodynamics-based continuum damage mechanics approach. Rigorous treatments of the classical and modern CDM approaches can be found in Refs [1, 23]. One key distinction in the damage evolution description for fatigue damage accumulation is cycle sensitivity. Unlike monotonic CDM evolution laws, fatigue damage laws must accommodate accumulation at subcritical load states [32]. In this section, the general description of the constitutive model is presented. The specific forms of the damage accumulation laws are described as part of the numerical verification section.

Consider the free energy per unit volume of the form:

$$\Psi^\eta = \Psi(\boldsymbol{\varepsilon}^\eta, \mathbf{D}^\eta) := \frac{1}{2} \boldsymbol{\varepsilon}^\eta : \mathbf{C}^\eta(\mathbf{D}^\eta) : \boldsymbol{\varepsilon}^\eta \quad (5)$$

where \mathbf{C}^η is the secant modulus tensor, that evolves as a function of the damage variables, \mathbf{D}^η ; and the colon indicates double inner product. The \mathbf{D}^η tensor tracks the evolution of the damage state at the material point:

$$\mathbf{D}^\eta = \{D_1^\eta, D_2^\eta, \dots, D_n^\eta\} \quad (6)$$

n is the number of damage variables, each of which tracks the evolution of a separate damage mechanism, possibly coupled to the others. Considering an isothermal response and assuming that the damage accumulation is slow enough to prohibit significant damage induced localized heating, the Clausius-Duhem inequality reduces to the mechanical dissipation:

$$-\dot{\Psi}^\eta + \boldsymbol{\sigma}^\eta : \dot{\boldsymbol{\varepsilon}}^\eta = \delta \geq 0 \quad (7)$$

in which, δ denotes the mechanical dissipation and, superposed dot indicates time derivative. Taking the time derivative of the free energy function in Eq. 5, and substituting it into the Clausius-Duhem inequality yields:

$$\dot{\boldsymbol{\varepsilon}}^\eta : [\boldsymbol{\sigma}^\eta - \mathbf{C}^\eta : \boldsymbol{\varepsilon}^\eta] - \frac{1}{2} \boldsymbol{\varepsilon}^\eta : \dot{\mathbf{C}}^\eta : \boldsymbol{\varepsilon}^\eta \geq 0 \quad (8)$$

Considering arbitrary strain rates in Eq. 8, we arrive at the constitutive relationship:

$$\boldsymbol{\sigma}^\eta = \mathbf{C}^\eta : \boldsymbol{\varepsilon}^\eta \quad (9)$$

along with the dissipative inequality

$$-\frac{1}{2}\boldsymbol{\varepsilon}^\eta : \dot{\mathbf{C}}^\eta : \boldsymbol{\varepsilon}^\eta = \delta \geq 0 \quad (10)$$

which implies that the time derivative of the secant modulus tensor should be negative definite to ensure thermodynamic consistency. By the chain rule the dissipation is expressed as:

$$\boldsymbol{\varepsilon}^\eta : (\mathbf{G}^\eta \cdot \mathbf{g}^\eta) : \boldsymbol{\varepsilon}^\eta = \delta \geq 0 \quad (11)$$

where,

$$\mathbf{G}^\eta := -\frac{1}{2} \frac{d\mathbf{C}^\eta}{d\mathbf{D}^\eta} \quad (12)$$

$$\dot{\mathbf{D}}^\eta = \mathbf{g}^\eta(\mathbf{D}^\eta, \boldsymbol{\varepsilon}, \mathbf{h}^\eta) \quad (13)$$

\mathbf{g}^η denotes the set of evolution equations for the damage variables, and \mathbf{h}^η are additional internal state variables defining the time evolution of the damage variables. The dissipation inequality imposes constraints on the form of these evolution equations. Let g_ζ^η denote the evolution equation of the damage variable D_ζ^η , and $\mathbf{G}_\zeta^\eta = (-1/2)\partial\mathbf{C}^\eta/\partial D_\zeta^\eta$, the dissipation becomes:

$$\boldsymbol{\varepsilon}^\eta : \left(\sum_{\zeta=1}^n \mathbf{G}_\zeta^\eta \cdot g_\zeta^\eta \right) : \boldsymbol{\varepsilon}^\eta = \delta \geq 0 \quad (14)$$

Taking \mathbf{G}_ζ^η to be positive semi-definite and since sum of positive semi-definite tensors is positive semi-definite, the dissipation inequality is satisfied for nonnegative evolution of the damage variables:

$$g_\zeta^\eta = g_\zeta(\mathbf{D}^\eta, \boldsymbol{\varepsilon}, \mathbf{h}^\eta) \geq 0 \quad (15)$$

In what follows, the analysis of the thermodynamic consistency of the discrete time evolution operators that results from time domain homogenization is performed by assuming that the evolution of the damage variables are nonnegative (i.e., Eq. 15) and that all derivatives of the tensor of secant moduli are positive semi-definite. In the discussion above, we adopted the formalism of strict dissipation [20], in which all damage induced inelastic deformation is dissipated. Some alternative thermodynamic damage formulations consider a defect energy component to the free energy, which is a function of the internal state variables, \mathbf{h}^η . The dissipation δ then takes an alternative form, which simply considers a part of mechanical dissipation to be stored in the material microstructure as an energetic contribution. The resulting evolution equations from either formulation are identical and the dissipative-energetic split of the mechanical dissipation is arbitrary, unless thermal contributions are included in the formulation [34].

The energy function (Eq. 5) is not an explicit function of the spatial coordinate, \mathbf{x} , which implies that the resulting damage model is local. Local damage formulations fail to capture the size scale effect and the numerical implementation of these formulations are known to exhibit mesh sensitivity when loading extends to the softening regime. Mesh sensitivity is characterized by localization of the strain and damage to a single finite element, regardless of the level of discretization. A number of thermodynamically consistent nonlocal damage formulations exist including gradient (e.g., [25]) and integral (e.g., [5]) type, and others (e.g., [33]). The demonstration of the thermodynamic consistency of the multiple time scale method is not affected by the nonlocal arguments, and this discussion is not included for the simplicity of the presentation.

3 Multiple time scales

Straightforward evaluation of the governing equations above using a standard incremental solution algorithm is computationally prohibitive. This is because the time to final failure is many orders of magnitude larger than the time step size needed to traverse a load cycle, and fatigue life prediction typically entails many millions of increments. Multiple time scale homogenization of the governing equation leads to more effective time integration algorithms, where only a subset of the load cycles throughout the loading history are resolved. To this end, two time scales are introduced: a *slow* time scale represented by the macrochronological coordinate, $t \in [0, t_l]$, and a *fast* time scale represented by the microchronological coordinate, $\tau \in [0, \tau_0]$. τ_0 is the scaled period of a single loading cycle. The micro- and macro- time scales are related by the scaling parameter, η , as:

$$\tau(t) = \frac{t}{\eta} \quad (16)$$

All fields that fluctuate in time (indicated with superscript η) are then expressed as a function of both the macrochronological and the microchronological time coordinates:

$$\phi^\eta(t) = \phi(t, \tau(t)) \quad (17)$$

in which, ϕ^η denotes an arbitrary response function. The time derivative of a fluctuating field is obtained using the chain rule.

$$\dot{\phi}^\eta(t) = \dot{\phi}(t, \tau(t)) = \frac{\partial \phi}{\partial t} + \frac{1}{\eta} \frac{\partial \phi}{\partial \tau} \quad (18)$$

When applied to the spatial scales, the computational homogenization procedure requires imposing particular boundary conditions defined over the unit spatial cell (i.e., representa-

tive volume) to fully describe the microscale problem. The boundary conditions must also ensure energy compatibility during the micro-macro transition (i.e., the Hill-Mandel condition). While a number of such boundary conditions have been proposed (see, e.g., [10, 27]), the most commonly used assumption is local periodicity of the response fields (i.e., displacements, stresses, strain, etc.) over the spatial cell. The generalization of the local periodicity condition to the time domain is usually not possible because of the presence of irreversible fields, such as the damage variables, in the underlying governing equations. For instance, the value of each damage variable only increases within a unit temporal cell (or microchronological cell) by Eq. 15. The magnitude of the damage variable at the end of a load cycle will therefore be higher than at the beginning, clearly violating the periodicity condition. Furthermore, the time domain evolution of the response fields is an initial value problem and the values of the response fields at the end of a microchronological cell are unknowns rather than prescribed fields. In contrast, defining the micro-macro transition still necessitates information on the evolution over the microchronological cell. The concept of almost periodicity, previously proposed in Ref. [29], resolves this difficulty by allowing small changes in the values of the response function at the boundaries of the microchronological cell. We denote the temporal averaging operator as:

$$\langle \phi \rangle_\tau(\mathbf{x}, t) := \frac{1}{\tau_0} \int_0^{\tau_0} \phi(\mathbf{x}, t, \tau) d\tau \quad (19)$$

The almost periodic temporal homogenization operator in the rate form is expressed as:

$$\dot{\tilde{\phi}} := \frac{\partial \mathcal{M}(\phi)}{\partial t} = \dot{\tilde{\phi}} + \dot{\phi}_{ap} \quad (20)$$

$$\dot{\phi}_{ap} = \frac{1}{\eta} \left\langle \frac{\partial \phi}{\partial \tau} \right\rangle_\tau \quad (21)$$

in which, (\cdot) is a time homogenization operator, and $\dot{\phi}_{ap}$ denotes the almost periodic component of the time rate of evolution of the temporally homogenized response field. Equation 20 implies that the time differentiation and the time homogenization operators do not commute. Choosing the temporal averaging operator as the time homogenization operator is natural and has been previously considered [29]. A more computationally convenient homogenization operator is the fixed point operator [12]:

$$\tilde{\phi}(t) = \phi(t, \tau^*) \quad (22)$$

in which, $\tau^* \in [0, \tau_0]$ is an arbitrary but fixed point within the microchronological cell. One attractive property of the fixed point operator compared to the averaging operator is its distributive property, which allows simple decomposition of the nonlinear fields (i.e.,

$$\phi = \psi\xi \rightarrow \tilde{\phi} = \tilde{\psi}\tilde{\xi}.$$

Herein, we demonstrate that the micro-macro transition is also accurate (but not exact) using an arbitrary choice of the fixed point. Of particular interest are power-like quantities ensuring accurate tracking of the dissipation and damage processes through time. Consider the micro-macro transition of the rate of strain energy defined using the almost periodic homogenization operation:

$$\Phi := \mathcal{M}(\boldsymbol{\sigma} : \dot{\boldsymbol{\epsilon}}) - \tilde{\boldsymbol{\sigma}} : \dot{\tilde{\boldsymbol{\epsilon}}} \approx 0 \quad (23)$$

Eq. 23, in which the terms on the right hand side denote the time homogenized strain energy rate at the micro-time scale and the energy rate computed using the mean stress and strain, respectively, is analogous to the Hill-Mandel condition used in spatial homogenization, but applied in the time domain and in rate form. Using the fixed point operator and its distributive property:

$$\mathcal{M}(\boldsymbol{\sigma} : \dot{\boldsymbol{\epsilon}}) = \tilde{\boldsymbol{\sigma}} : \dot{\tilde{\boldsymbol{\epsilon}}} = \boldsymbol{\sigma}(t, \tau^*) \left[\frac{\partial \boldsymbol{\epsilon}(t, \tau^*)}{\partial t} + \frac{1}{\eta} \frac{\partial \boldsymbol{\epsilon}(t, \tau^*)}{\partial \tau} \right] \quad (24)$$

and

$$\tilde{\boldsymbol{\sigma}} : \dot{\tilde{\boldsymbol{\epsilon}}} = \boldsymbol{\sigma}(t, \tau^*) \left[\frac{\partial \boldsymbol{\epsilon}(t, \tau^*)}{\partial t} + \frac{1}{\eta} \left\langle \frac{\partial \boldsymbol{\epsilon}(t, \tau)}{\partial \tau} \right\rangle_\tau \right] \quad (25)$$

Substituting Eqs. 24 and 25 into Eq. 23:

$$\Phi = \frac{1}{\eta} \tilde{\boldsymbol{\sigma}} : \left[\frac{\partial \boldsymbol{\epsilon}(t, \tau^*)}{\partial \tau} - \frac{\boldsymbol{\epsilon}(t, \tau_0) - \boldsymbol{\epsilon}(t, 0)}{\tau_0} \right] \quad (26)$$

Expanding the time derivative of the strain with respect to the fast time scale using the Taylor series expansion up to the third order, we obtain:

$$\Phi = \frac{\tau_0 - 2\tau^*}{\eta} \tilde{\boldsymbol{\sigma}} : \frac{\partial^2 \boldsymbol{\epsilon}(t, \tau^*)}{\partial \tau^2} \quad (27)$$

which implies the micro-macro transition is satisfied up to the third order term when the fixed point operator is chosen to be the mid-point (i.e., $\tau^* = \tau_0/2$). Despite a slightly larger error, the choice of $\tau^* = 0$ is computationally more convenient since the fixed point operator then coincides with the initial value of the microstructure cell problem and a standard incremental solution strategy is achieved. Provided that the evolution of the response fields is relatively smooth, the proposed operator homogenizes the microchronological scale response with reasonable accuracy.

The boundary tractions and displacements are prescribed such that they can be decom-

posed into slow and fast loading components as follows:

$$\hat{\mathbf{u}}^\eta(\mathbf{x}, t) = \hat{\mathbf{u}}(\mathbf{x}, t, \tau) = \hat{\mathbf{u}}_0(\mathbf{x}, t) + \hat{\mathbf{u}}_1(\mathbf{x}, \tau) \quad \mathbf{x} \in \Gamma_u \quad (28)$$

$$\hat{\mathbf{t}}^\eta(\mathbf{x}, t) = \hat{\mathbf{t}}(\mathbf{x}, t, \tau) = \hat{\mathbf{t}}_0(\mathbf{x}, t) + \hat{\mathbf{t}}_1(\mathbf{x}, \tau) \quad \mathbf{x} \in \Gamma_t \quad (29)$$

such that $\hat{\mathbf{u}}_1(\mathbf{x}, 0) = \mathbf{0}$ and $\hat{\mathbf{t}}_1(\mathbf{x}, 0) = \mathbf{0}$ (Fig. 1). The vanishing initial conditions of the prescribed tractions and displacements are not a restriction on the loading. For instance, for a nonhomogeneous initial prescribed displacement, $\hat{\mathbf{u}}_1(\mathbf{x}, \tau) = c$, the slow and fast loading components can be shifted as: $\hat{\mathbf{u}}_0^{\text{new}} \equiv \hat{\mathbf{u}}_0 + c$ and $\hat{\mathbf{u}}_1^{\text{new}} \equiv \hat{\mathbf{u}}_1 - c$ to bring the overall prescribed load to the required form.

4 Time scale homogenization

In this section, the original boundary value problem that defines the evolution of failure under the fatigue loading is decomposed into microchronological and macrochronological problems based on the time scale homogenization with almost periodic and fixed point operators. The microchronological problem is an initial boundary value problem (IBVP) that defines the evolution of the response subjected to a single microchronological cell (i.e., a single period of fast time scale loading), whereas the macrochronological problem is the homogenized IBVP, which provides the system response under slowly varying loads. Application of time homogenization results in a fully coupled pair of micro- and macrochronological problems. We also present a simplification, which leads to a partially decoupling and accelerated time integration of the multiscale problems.

4.1 Microchronological IBVP

Let $\phi^m(\mathbf{x}, \tau) := \phi(\mathbf{x}, t^*, \tau)$ denote a response field at a fixed but arbitrary macrochronological time, t^* . The microchronological IBVP is obtained by stating the original governing equations at the fixed macrochronological time, t^* . Accordingly, the equilibrium equation for the microchronological problem becomes:

$$\nabla \cdot \boldsymbol{\sigma}^m(\mathbf{x}, \tau) + \mathbf{b}(\mathbf{x}) = \mathbf{0}; \quad \mathbf{x} \in \Omega, \quad \tau \in [0, \tau_0] \quad (30)$$

in which, the stress, $\boldsymbol{\sigma}^m$, is obtained by applying Eq. 17 to the original constitutive relationship (Eq. 9) at $t = t^*$:

$$\boldsymbol{\sigma}^m(\mathbf{x}, \tau) = \mathbf{C}^m(\mathbf{x}; \mathbf{D}^m(\tau)) : \boldsymbol{\varepsilon}^m(\mathbf{x}, \tau) \quad (31)$$

The strain, $\boldsymbol{\varepsilon}^m$ is related to the displacement field using the small strain kinematic relationship by applying Eq. 17 to Eq. 2 at $t = t^*$:

$$\boldsymbol{\varepsilon}^m(\mathbf{x}, \tau) = \nabla^s \mathbf{u}^m(\mathbf{x}, \tau) \quad (32)$$

The evolution equation of the microchronological damage tensor, \mathbf{D}^m is obtained by the asymptotic analysis of the damage evolution laws. Applying Eq. 18 to Eq. 13 and collecting the same order terms with respect to the scaling parameter, η yields:

$$O(\eta^{-1}) : \frac{\partial \mathbf{D}}{\partial \tau}(\mathbf{x}, t, \tau) = \mathbf{g}^0(\mathbf{x}, t, \tau; \mathbf{D}, \boldsymbol{\varepsilon}, \mathbf{h}) \quad (33a)$$

$$O(1) : \frac{\partial \mathbf{D}}{\partial t}(\mathbf{x}, t, \tau) = \mathbf{g}^1(\mathbf{x}, t, \tau; \mathbf{D}, \boldsymbol{\varepsilon}, \mathbf{h}) \quad (33b)$$

The decomposition of the damage evolution equation implies that the damage evolution functions can be expressed as an asymptotic series, i.e.: $\mathbf{g} = (1/\eta)\mathbf{g}^0 + \mathbf{g}^1$. An evolution equation of the general form:

$$\mathbf{g} = \mathbf{P}(\mathbf{D}, \boldsymbol{\varepsilon}, \mathbf{h}) \cdot \dot{\mathbf{h}} \quad (34)$$

where \mathbf{P} is of order $O(1)$, satisfies the above constraint, and is admissible. We note that when the almost periodic homogenization operator is applied to the damage evolution expansion, the resulting terms are of the same order of magnitude, $O(1)$, in view of the definition of almost periodicity. Evaluating Eq. 33a at $t = t^*$ yields the evolution equation for \mathbf{D}^m with respect to the microchronological time scale:

$$\frac{\partial \mathbf{D}^m}{\partial \tau}(\mathbf{x}, \tau) = \mathbf{g}^{0m}(\mathbf{x}, \tau; \mathbf{D}^m, \boldsymbol{\varepsilon}^m, \mathbf{h}^m) \quad (35)$$

The boundary conditions for the microchronological problem are obtained by evaluating Eqs. 28 and 29 at $t = t^*$.

$$\mathbf{u}^m(\mathbf{x}, \tau) = \hat{\mathbf{u}}_0^m(\mathbf{x}) + \hat{\mathbf{u}}_1(\mathbf{x}, \tau) \quad \mathbf{x} \in \Gamma_u \quad (36)$$

$$\mathbf{t}^m(\mathbf{x}, \tau) = \hat{\mathbf{t}}_0^m(\mathbf{x}) + \hat{\mathbf{t}}_1(\mathbf{x}, \tau) \quad \mathbf{x} \in \Gamma_t \quad (37)$$

The initial conditions of the microchronological problem are established using the fixed point homogenization operator and constitute the coupling between the micro- and macrochronological problems. When the fixed point operator is chosen as $\tau^* = 0$, the initial state of the microchronological problem coincides with the homogenized state:

$$\mathbf{u}^m(\mathbf{x}, 0) = \tilde{\mathbf{u}}(\mathbf{x}, t^*), \quad \mathbf{D}^m(\mathbf{x}, 0) = \tilde{\mathbf{D}}(\mathbf{x}, t^*), \quad \mathbf{h}^m(\mathbf{x}, 0) = \tilde{\mathbf{h}}(\mathbf{x}, t^*); \quad \mathbf{x} \in \Omega \quad (38)$$

in which, $\tilde{\mathbf{u}}$, $\tilde{\mathbf{D}}$ and $\tilde{\mathbf{h}}$ are evaluated within the macrochronological IBVP defined below. Equations 30-38 along with the explicit form of the evolution equations fully define the microchronological IBVP as a function of the macrochronological response. When an alternative fixed point operator is chosen ($\tau^* \neq 0$), the initial conditions of the microchronological problem remain unknown. The IBVP is closed by considering the fixed point state as a constraint:

$$\mathbf{u}^m(\mathbf{x}, \tau^*) = \tilde{\mathbf{u}}(\mathbf{x}, t^*), \quad \mathbf{D}^m(\mathbf{x}, \tau^*) = \tilde{\mathbf{D}}(\mathbf{x}, t^*), \quad \mathbf{h}^m(\mathbf{x}, \tau^*) = \tilde{\mathbf{h}}(\mathbf{x}, t^*); \quad \mathbf{x} \in \Omega \quad (39)$$

In the context of a time incremental solution algorithm, the microchronological problem, using Eq. 39, requires an iterative solution scheme, since the initial conditions of the problem are also unknowns. Despite the higher accuracy that can be achieved by using a nonzero fixed point operator (i.e., Eq. 27), the computational complexity of the resulting formulation is high. Therefore, $\tau^* = 0$ is the computationally efficient choice, and adopted herein.

4.2 Macrochronological IBVP

The governing equations of the macrochronological problem are obtained by applying the fixed point operator to the original governing equations. The equilibrium and kinematic equations become:

$$\nabla \cdot \tilde{\boldsymbol{\sigma}}(\mathbf{x}, t) + \mathbf{b}(\mathbf{x}) = \mathbf{0} \quad (40)$$

$$\tilde{\boldsymbol{\varepsilon}}(\mathbf{x}, t) = \nabla^s \tilde{\mathbf{u}}(\mathbf{x}, t) \quad (41)$$

Applying the fixed point operator to the constitutive relationship in Eq. 9 and using the distributive property of the fixed point operator yields:

$$\tilde{\boldsymbol{\sigma}}(\mathbf{x}, t) = \tilde{\mathbf{C}}(\mathbf{x}; \tilde{\mathbf{D}}(t)) : \tilde{\boldsymbol{\varepsilon}}(\mathbf{x}, t) \quad (42)$$

The evaluation of the time homogenized secant moduli, $\tilde{\mathbf{C}}$, requires the time evolution of the time homogenized damage variables, $\tilde{\mathbf{D}}$. The macroscale evolution functions for the damage variables are obtained through the almost periodic operator. Applying Eq. 20 to the damage tensor, and considering Eqs. 33a-b:

$$\dot{\tilde{\mathbf{D}}}(\mathbf{x}, t) = \tilde{\mathbf{g}}^1(\mathbf{x}, t; \mathbf{D}, \boldsymbol{\varepsilon}, \mathbf{h}) + \dot{\mathbf{D}}_{ap}(\mathbf{x}, t) \quad (43)$$

in which, the almost periodic component is obtained based on the microchronological time evolution of the damage variables:

$$\dot{\mathbf{D}}_{\text{ap}}(\mathbf{x}, t) = \frac{1}{\eta} \langle \mathbf{g}^0 \rangle_\tau \quad (44)$$

The boundary conditions are obtained by applying the fixed point operator ($\tau^* = 0$) to the boundary conditions and considering the homogeneity conditions imposed on the prescribed fields (i.e., $\hat{\mathbf{u}}_1(\mathbf{x}, 0) = \mathbf{0}$ and $\hat{\mathbf{t}}_1(\mathbf{x}, 0) = \mathbf{0}$):

$$\tilde{\mathbf{u}}(\mathbf{x}, t) = \hat{\mathbf{u}}_0(\mathbf{x}, t) \quad \mathbf{x} \in \Gamma_u \quad (45)$$

$$\tilde{\boldsymbol{\sigma}}(\mathbf{x}, t) \cdot \mathbf{n}(\mathbf{x}) = \hat{\mathbf{t}}_0(\mathbf{x}, t) \quad \mathbf{x} \in \Gamma_t \quad (46)$$

The initial state of the macrochronological IBVP follows from the initial state of the original problem. The initial stress, displacement and the internal state variables of the homogenized fields are taken as zero.

4.3 Quasi-linear approximation of the microchronological problem

The microchronological IBVP defined by Eqs. 30-32 and 35-38 is nonlinear and evaluation of the system of equations over a large domain requires significant computational effort, particularly since the microchronological problem is evaluated at multiple discrete macrochronological time steps (i.e., each t^*) throughout the fatigue life of the structure. We seek to significantly improve the efficiency of the ensuing life prediction methodology by considering a simplification in the evaluation of the microchronological problem. The idea of almost periodicity tacitly presumes that the change in the response fields over a single microchronological cell is small. In line with this assumption, the equilibrium state over a single microchronological cell is taken to be unaffected by the variation in the damage state:

$$\boldsymbol{\sigma}^m(\mathbf{x}, \tau) \approx \mathcal{C}^m(\mathbf{x}; \mathbf{D}^m(\tau^*)) : \boldsymbol{\varepsilon}^m(\mathbf{x}, \tau) \quad (47)$$

where, \mathcal{C}^m is the value of the secant modulus tensor evaluated at the fixed point, τ^* . The secant modulus tensor is therefore taken to be constant over a single microchronological cell. By this simplification, the microchronological equilibrium is expressed as:

$$\nabla \cdot [\mathcal{C}^m(\mathbf{x}) : \nabla^s \mathbf{u}^m(\mathbf{x}, \tau)] + \mathbf{b}(\mathbf{x}) = \mathbf{0}; \quad \mathbf{x} \in \Omega, \quad \tau \in [0, \tau_0] \quad (48)$$

subjected to the boundary and initial conditions stated in Eqs. 36-38. The microchronological equilibrium equation decouples from the microchronological damage evolution equations (i.e., Eq. 35). Two major simplifications arise by considering the quasi-linear approximation to the

microchronological equilibrium. First, when the loading within the microchronological cell is proportional, the evaluation of the microchronological equilibrium reduces to obtaining the linear elastic responses subjected to unit loads along the direction of the prescribed boundary loads, and employing superposition to compute the displacement, strain and stress response under the prescribed boundary loading. Second, while the damage evolution equations are nonlinear, they are local ODEs (in view of the local character of the damage evolution functions) to be evaluated independent of each other at each integration point throughout the domain. Parallelization of the microchronological damage evolution computation is therefore trivial and completely scalable.

5 Computational implementation

The framework outlined in this manuscript was implemented and numerically verified. The implementation of the micro- and macro-chronological problems defined in Section 4 is performed by considering: (1) The fixed point homogenization operator set as $\tau^* = 0$; and (2) the quasi-linear approximation of the micro-chronological problem. The implementation uses the commercial finite element software, Abaqus. Choosing the fixed point operator as $\tau^* = 0$ implies that the macrochronological state at a fixed macrochronological time coincides with the initial state of a microchronological problem. Along with forward discretization of the almost periodic damage rate, the resulting computational algorithm is staggered such that the micro- and macro- problems are evaluated in turn, without a need for micro-macro convergence iterations. Employing the approximation for the microchronological problem introduced in Section 4.3, the microchronological problems themselves are quasilinear, whereas the macrochronological problem remains nonlinear and is evaluated using an iterative scheme. In this section, we first present an adaptive macrochronological time stepping methodology and the resulting computational algorithm. We then present an analysis of the implementation for thermodynamic consistency. In particular, the dissipative inequality is checked, and conditions to ensure the thermodynamic consistency are stated.

5.1 Adaptive macrochronological time stepping

The details of the adaptive macrochronological time stepping algorithm are described in Ref. [12]. In this manuscript, we summarize the algorithm to provide the context for the thermodynamic analysis detailed in the next section. The macrochronological time step size is chosen as a function of damage accumulation under cyclic loading (i.e., microchronological cell), which implies that the homogenized damage accumulation rate is largely due to the almost periodic contribution.

The proposed computational algorithm involves solving the macrochronological problem by incrementally stepping through macrochronological time in increments adaptively chosen throughout the life of the body (e.g., t_0, t_1, t_2, \dots). In space, the macrochronological problem is discretized and solved using the finite element method. Let $\mathbf{x}_1, \mathbf{x}_2, \dots, \mathbf{x}_{n_g}$ be the coordinates of the Gauss points within the discretized domain. $\mathbf{D}'(t)$ is the set of all almost periodic rates of damage at the integration points:

$$\mathbf{D}'(t) = [\dot{\mathbf{D}}_{\text{ap}}(\mathbf{x}_1, t), \dot{\mathbf{D}}_{\text{ap}}(\mathbf{x}_2, t), \dots, \dot{\mathbf{D}}_{\text{ap}}(\mathbf{x}_{n_g}, t)] \quad (49)$$

which is assumed to vary smoothly during a macrochronological step: (i.e., $t_i \leq t < t_{i+1}$). The i^{th} macrochronological time step is denoted as: $\Delta t_i = t_{i+1} - t_i$. The $\mathbf{D}'(t)$ within $t_i \leq t < t_{i+1}$ is approximated with a linear function constructed from $\mathbf{D}'(t_i)$ and $\mathbf{D}'(t_{i-1})$ as follows:

$$\mathbf{D}'(t) \approx \mathbf{D}'(t_i) + \frac{\Delta t}{\Delta t_{i-1}} (\mathbf{D}'(t_i) - \mathbf{D}'(t_{i-1})) ; \quad t_i \leq t < t_{i+1} \quad (50)$$

We also consider the following simpler constant approximation of $\mathbf{D}'(t)$:

$$\mathbf{D}'(t) \approx \mathbf{D}'(t_i) \quad (51)$$

The approximation of the almost periodic rates using Eq. 50 is a forward discretization; i.e., does not include information beyond, t_i . This approximation, along with the specific choice of the fixed point operator ($\tau^* = 0$) leads to an explicit computational algorithm. The change in the almost periodic components of the damage variables during the macrochronological increment are approximated by integrating Eq. 50:

$$\Delta \mathbf{D}_i \approx \int_0^{\Delta t_i} \mathbf{D}'(t) dt = \mathbf{D}'(t_i) \Delta t_i + \frac{\Delta t_i^2}{2 \Delta t_{i-1}} (\mathbf{D}'(t_i) - \mathbf{D}'(t_{i-1})) \quad (52)$$

and integrating Eq. 51 yields a similar result for the constant approximation.

$$\Delta \mathbf{D}_i \approx \int_0^{\Delta t_i} \mathbf{D}'(t) dt = \mathbf{D}'(t_i) \Delta t_i \quad (53)$$

The macrochronological time step size, Δt_i , is adaptively chosen by limiting the difference in the damage change predicted by the constant and linear approximations of $\mathbf{D}'(t)$ (Eqs. 50 and 51).

$$\text{find } \Delta t_i \text{ s.t.} ; \quad \left\| \frac{\Delta t_i^2}{2 \Delta t_{i-1}} (\mathbf{D}'(t_i) - \mathbf{D}'(t_{i-1})) \right\|_p \leq \text{tol} \quad (54)$$

where tol is the damage accumulation tolerance, and $\|\cdot\|_p$ denotes the discrete l_p -norm. Comparing higher and lower order methods to adaptively choose the stepsize is also com-

monly used for adaptive Runge-Kutta methods. The following alternative adaptive step size criterion is used for the constant approximation of $\mathbf{D}'(t)$.

$$\Delta t_i = \Delta D_p / \|\mathbf{D}'(t_i)\|_p \quad (55)$$

where ΔD_p is a numerical parameter controlling the restrictiveness of the adaptive step size.

The multiscale solution strategy is implemented as follows. A driver program (implemented in Python) controls the evaluation of the microchronological and macrochronological problems at each macro time step. The driver also sets the initial conditions for the microchronological problems at each macro time step and computes the macrochronological time step size using Eq. 54 or 55. The evaluation of a microchronological step requires only a single linear perturbation due to the quasi-linear approximation. The microchronological damage evolution is computed by integrating the microchronological damage evolution laws (Eq. 35) for each integration point using strain values determined from the linear perturbation. The almost periodic damage rates computed within the microchronological problem solution is stored in an external database, and in turn used by the driver to compute the time step sizes. No microchronological equilibrium step beyond the linear perturbation step is needed. The macrochronological problem is evaluated using the incremental, nonlinear solver within Abaqus. The user material subroutine (UMAT) feature of Abaqus is utilized to implement the macrochronological constitutive law (Eq. 42), and the associated damage evolution laws (Eq. 43).

The computational algorithm for determining the structural response over the lifetime of a structure is summarized as below:

1. Evaluate a microchronological step without the quasi-linear approximation to determine $\mathbf{D}'(t_0)$.
2. Evaluate a microchronological step without the quasi-linear approximation to determine $\mathbf{D}'(t_1)$ using the final state of the previous evaluation as initial conditions.
3. Initialize $i = 1$.
4. Check for structural failure and repeat until failure is detected.
 - (a) Calculate Δt_i using Eq. 54 (or Eq. 55).
 - (b) Calculate $\mathbf{D}'(t)$ using Eq. 50 (or Eq. 51).
 - (c) Evaluate a macrochronological step.
 - (d) Evaluate a microchronological step with the quasi-linear approximation to determine $\mathbf{D}'(t_{i+1})$ using the final state of the macrochronological step as initial conditions.

5. End

(e) Increment i

5.2 Thermodynamic consistency

Satisfying the dissipative inequality using the adaptive time stepping methodology imposes an additional constraint on the macrochronological time step size. Considering the two term asymptotic expansion of the damage evolution function, Eq. 13, and the non-negative constraint on the evolution equation imposed by the dissipation inequality (i.e., Eq. 15) yields:

$$\frac{1}{\eta} g_\zeta^0(\mathbf{D}, \boldsymbol{\varepsilon}, \mathbf{h}) + g_\zeta^1(\mathbf{D}, \boldsymbol{\varepsilon}, \mathbf{h}) \geq 0 \quad (56)$$

for each damage variable, ζ . The first and the second terms in Eq. 56 denote damage accumulation induced by the fast and slow varying loads, respectively. Since the inequality must be satisfied for the cases of pure fatigue loading (i.e., $g_\zeta^1 = 0$) and pure monotonic loading (i.e., $g_\zeta^0 = 0$), the thermodynamic consistency implies:

$$g_\zeta^0(\mathbf{D}, \boldsymbol{\varepsilon}, \mathbf{h}) \geq 0; \quad g_\zeta^1(\mathbf{D}, \boldsymbol{\varepsilon}, \mathbf{h}) \geq 0 \quad (57)$$

The macrochronological damage evolution law, with the quadratic time stepping approximation, results in the following expression ($t_i \leq t < t_{i+1}$): By considering Eqs. 33a, 43, 44, 49, and 50, we arrive at the following expression:

$$\dot{\tilde{\mathbf{D}}}(\mathbf{x}, t) = \tilde{\mathbf{g}}^1(\mathbf{x}, t; \tilde{\mathbf{D}}, \tilde{\boldsymbol{\varepsilon}}, \tilde{\mathbf{h}}) + \frac{1}{\eta} \left\langle \left(1 + \frac{\Delta t_i}{\Delta t_{i-1}}\right) \frac{\partial \mathbf{D}}{\partial \tau}(\mathbf{x}, t_i, \tau) - \left(\frac{\Delta t_i}{\Delta t_{i-1}}\right) \frac{\partial \mathbf{D}}{\partial \tau}(\mathbf{x}, t_{i-1}, \tau) \right\rangle_\tau \quad (58)$$

To ensure the thermodynamic consistency of the proposed time stepping strategy, it suffices to show that the two terms on the right hand side of Eq. 58 are nonnegative. By Eq. 57b it is trivial to see that the first term, $\tilde{\mathbf{g}}^1$, is nonnegative. To ensure that the second term remains positive, we set the kernel of the integral to be positive (for all \mathbf{x}):

$$\begin{aligned} \frac{\partial \mathbf{D}}{\partial \tau}(t_i, \tau) \left(1 + \frac{\Delta t_i}{\Delta t_{i-1}}\right) - \frac{\partial \mathbf{D}}{\partial \tau}(t_{i-1}, \tau) \left(\frac{\Delta t_i}{\Delta t_{i-1}}\right) \\ = \frac{\partial \mathbf{D}}{\partial \tau}(t_i, \tau) + \left(\frac{\partial \mathbf{D}}{\partial \tau}(t_i, \tau) - \frac{\partial \mathbf{D}}{\partial \tau}(t_{i-1}, \tau)\right) \frac{\Delta t_i}{\Delta t_{i-1}} \geq \mathbf{0} \end{aligned} \quad (59)$$

By Eq. 57a:

$$\frac{\partial \mathbf{D}}{\partial \tau}(t_i, \tau) \geq \mathbf{0} \quad (60)$$

Considering the following time step size constraint guarantees that Eq. 59 is satisfied.

$$\Delta t_i = \min_{j=1,\dots,n} \left\{ \Delta t_{i-1} \frac{\frac{\partial D^j}{\partial \tau}(t_i, \tau)}{\frac{\partial D^j}{\partial \tau}(t_{i-1}, \tau) - \frac{\partial D^j}{\partial \tau}(t_i, \tau)} \right\} \quad (61)$$

and $\Delta t_i \geq 0$. If for any j 's $\frac{\partial D^j}{\partial \tau}(t_i, \tau) = 0$, then Eq. 61 would provide $\Delta t_i = 0$. We construct two sets of integers $A = \{j \in 1, \dots, n | \frac{\partial D^j}{\partial \tau}(t_i, \tau) = 0\}$ and $B = \{j \in 1, \dots, n | \frac{\partial D^j}{\partial \tau}(t_i, \tau) \neq 0\}$. Eq. 61 then becomes

$$\Delta t_i = \min_B \left\{ \Delta t_{i-1} \frac{\frac{\partial D^j}{\partial \tau}(t_i, \tau)}{\frac{\partial D^j}{\partial \tau}(t_{i-1}, \tau) - \frac{\partial D^j}{\partial \tau}(t_i, \tau)} \right\} \quad (62)$$

and we fix $\dot{\tilde{D}}^j(\mathbf{x}, t) = 0$ for every j in A . Therefore, Eq. 62 is maintained alongside Eq. 54 as an additional constraint on the size of Δt_i , thereby ensuring satisfaction of the dissipative inequality.

6 Model Verification

In this section, the proposed multiple time scale homogenization formulation with the accelerated time integration scheme is numerically verified. The proposed model is compared to the direct cycle-by-cycle simulations, in which the standard nonlinear time increment strategy that resolves every load cycle throughout the loading history is employed. The first verification case is concerned with the time domain integration only, based on the response of a 1-D nonlinear spring model. The second verification case includes a spatially multiscale 3-D damage evolution model for composite materials.

6.1 One-dimensional nonlinear spring model

The governing equations for the one-dimensional nonlinear spring problem are shown in Box 1. σ^η is the stress on the spring, ε^η the strain; u^η the displacement, $T^\eta(t)$ is the applied traction, and L is the length of the spring. D^η denotes the damage state of the spring, E the Young's modulus, g is the evolution law for the damage variable. T_0 and T_1 are slowly varying and cyclic applied tractions, respectively.

The fatigue sensitive damage evolution function is given as [17]:

$$g(\varepsilon^\eta(t), D^\eta(t)) = \left[\frac{\Phi^\eta(t)}{D^\eta(t)} \right]^\gamma \langle \dot{\Phi}^\eta(t) \rangle_+ \quad (68)$$

where $\langle \cdot \rangle_+ = [(\cdot) + |\cdot|]/2$ denotes the Macaulay brackets. γ is a material parameter that

controls the sensitivity of the damage accumulation model to the fatigue loads.

$$\Phi^\eta(v^\eta(t)) = \frac{\arctan(av^\eta(t) - b) + \arctan(b)}{\frac{\pi}{2} + \arctan(b)} \quad (69)$$

where, a and b are material parameters that control the damage accumulation under monotonic loads. The damage accumulates as a function of the damage equivalent strain, v^η :

$$v^\eta(\varepsilon^\eta(t)) = \sqrt{\frac{E}{2}} |\varepsilon^\eta(t)| \quad (70)$$

Applying the multiple time scale homogenization method to the governing equations of the nonlinear spring yields the micro- and macrochronological problems, which are summarized in Boxes 2 and 3, respectively.

In all simulations considered in this section, the following parameters are used: $L = 1.0$ m, $E = 10$ MPa, $a = 0.1$, $b = 12.0$, and $\gamma = 2.5$. In the first set of simulations, a sinusoidal loading of the following form is imparted on the spring:

$$T(t, \tau) = T_0(t) + T_1(\tau) \quad (81)$$

where,

$$T_0(t) = \frac{\sigma_{\max} + \sigma_{\min}}{2} + \frac{\sigma_{\max} - \sigma_{\min}}{2} \sin(-2\pi c) \quad (82)$$

$$T_1(\tau) = \frac{\sigma_{\max} - \sigma_{\min}}{2} [\sin(2\pi(\tau - c)) - \sin(-2\pi c)] \quad (83)$$

The maximum and minimum values of the applied loading are denoted as σ_{\max} and σ_{\min} , respectively. $0 \leq c < 1$ is a phase shift factor, which changes the initial state of the loading while leaving the loading rate and the minimum and maximum applied tractions unchanged. Introducing the phase shift is a convenient way to explore the effect of the choice for the

$\text{Equilibrium: } \sigma^\eta(t) = T^\eta(t) \quad (63)$ $\text{Strain-displacement: } \varepsilon^\eta(t) = \frac{u^\eta(t)}{L} \quad (64)$ $\text{Constitutive relationship: } \sigma^\eta(t) = [1 - D^\eta(t)] E \varepsilon^\eta(t) \quad (65)$ $\text{Damage evolution: } \dot{D}^\eta(t) = g(\varepsilon^\eta(t), D^\eta(t)) \quad (66)$ $\text{Initial conditions: } D(t=0) = 0; \quad u(t=0) = 0 \quad (67)$
--

Box 1: Governing equations of the one-dimensional nonlinear spring problem.

Find $u^m(\tau)$ and $D^m(\tau)$ in $\tau \in [0, \tau_0]$ such that:

$$\text{Equilibrium: } \sigma^m(\tau) = T_0^m + T_1(\tau) \quad (71)$$

$$\text{Constitutive relationship: } \sigma^m(\tau) = [1 - D^m(0)] E \varepsilon^m(\tau) \quad (72)$$

$$\text{Strain-displacement: } \varepsilon^m(\tau) = \frac{u^m(\tau)}{L} \quad (73)$$

$$\text{Damage evolution: } \frac{\partial D^m(\tau)}{\partial \tau} = \left[\frac{\Phi^m(v^m(\tau))}{D^m(\tau)} \right]^\gamma \left\langle \frac{\partial \Phi^m(v^m(\tau))}{\partial \tau} \right\rangle_+ \quad (74)$$

$$\text{Initial conditions: } D^m(\tau = 0) = \tilde{D}(t^*); u^m(\tau = 0) = \tilde{u}(t^*) \quad (75)$$

Box 2: Governing equations of the microchronological nonlinear spring problem.

Find $\tilde{u}(t)$ and $\tilde{D}(t)$ in $t \in [0, t_f]$ such that:

$$\text{Equilibrium: } \tilde{\sigma}(t) = T_0(t) \quad (76)$$

$$\text{Constitutive relationship: } \tilde{\sigma}(t) = [1 - \tilde{D}(t)] E \tilde{\varepsilon}(t) \quad (77)$$

$$\text{Strain-displacement: } \tilde{\varepsilon}(t) = \frac{\tilde{u}(t)}{L} \quad (78)$$

$$\text{Damage evolution: } \dot{\tilde{D}}(t) = \left[\frac{\tilde{\Phi}(\tilde{v}(t))}{\tilde{D}(t)} \right]^\gamma \left\langle \frac{\partial \tilde{\Phi}(\tilde{v}(t))}{\partial t} \right\rangle_+ + \dot{D}_{ap}(t) \quad (79)$$

$$\text{Initial conditions: } \tilde{D}(t = 0) = 0; \quad \tilde{u}(t = 0) = 0 \quad (80)$$

Box 3: Governing equations of the macrochronological nonlinear spring problem.

fixed point operator as a function of the level of the applied traction. For instance, the choice of $c = 1/4$ implies that $T_0(t) = \sigma_{\min}$, and $c = 3/4$ leads to $T_0(t) = \sigma_{\max}$. Since the fixed point operator is set to $\tau^* = 0$, the position of the fixed point operator coincides with the minimum and maximum of the loading profile, respectively.

The performance of the methodology is tested at three different loading magnitudes with the load shift factors of $c = 1/4$ and $c = 3/4$. The maximum applied load amplitude, σ_{\max} , was set to 330 kPa, 265 kPa, and 205 kPa with an R -ratio of 0.1 (i.e., $\sigma_{\min} = 0.1\sigma_{\max}$) for each case. In these simulations, the macrochronological time increment is set to the length of a single loading cycle; i.e., the adaptive step size selection was not used. Since no cycle jump is considered, the sources of errors are limited to the choice of the fixed point operator and the accelerated time integration scheme only (i.e., Eq. 72).

Figures 2-4 show the evolution of damage in the spring as a function of the number of load

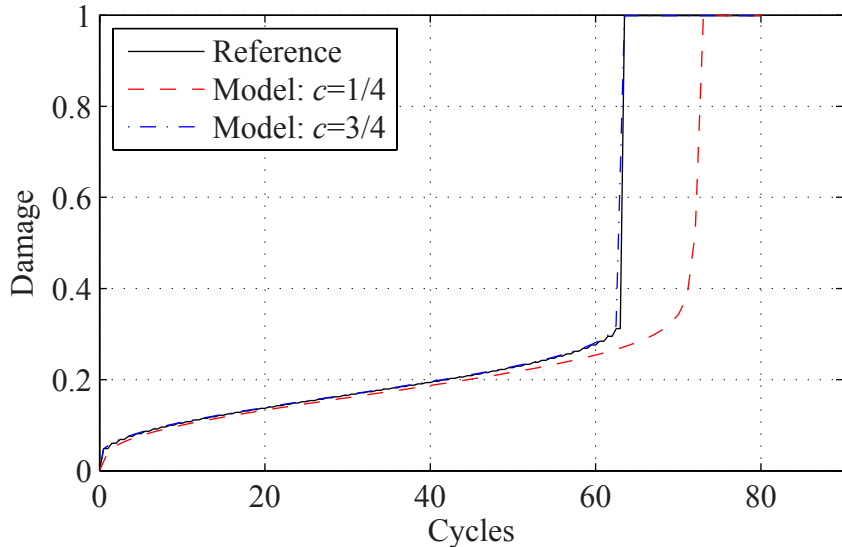


Figure 2: Nonlinear spring subjected to cyclic loading with maximum amplitude of 330 kPa.

cycles for the high, medium, and low amplitude loading, respectively. The high amplitude loading corresponds to low cycle fatigue ($N_f = 63$, N_f denotes number of cycles to failure), whereas the low amplitude loading corresponds to the high cycle fatigue ($N_f = 8599$). In the case of low cycle fatigue (Fig. 2), the choice for the phase shift factor (i.e., fixed point operator) has a significant effect on the accuracy. The choice of $c = 3/4$, which implies that the fixed point operator coincides with the maximum applied traction, leads to an accurate description of the damage evolution using the accelerated time integration scheme, whereas $c = 1/4$ displays a slightly lower accuracy. As the number of cycles to failure is increased (Figs. 3 and 4), the proposed approach converges to the reference solution, regardless of the phase shift (i.e., the position of fixed point operator with respect to the loading amplitude) fatigue load suggesting that for high cycle fatigue the effect of the phase shift on the solution accuracy is not significant. In the remainder of the simulations, $c = 3/4$ is employed.

Figures 2-4 also show the effect of the value of the scaling parameter on the performance of the proposed multiscale approach. The scaling parameter is a function of the ratio between cycle duration, which is kept constant, and the total time to failure, which increases as the load is reduced. Therefore, the scaling parameter is reduced from Figures 2-4. The increase in accuracy as the scaling parameter is reduced points to convergence as $\eta \rightarrow 0$.

A second set of simulations was conducted to assess the accuracy of the proposed method including the adaptive time stepping strategy in the context of linear and quadratic macrochronological time stepping criteria. Figure 5 shows the evolution of damage as a function of the number of loading cycles when a linear time stepping criterion is used. The simulations were performed by setting $\sigma_{\max} = 125$ kPa and R-ratio = 0.1. At time step, i , the time increment

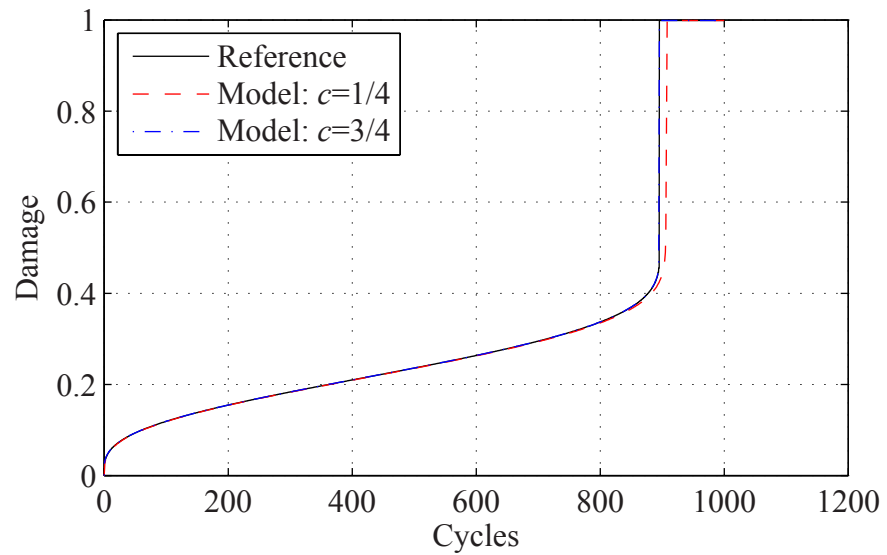


Figure 3: Nonlinear spring subjected to cyclic loading with maximum amplitude of 265 kPa.

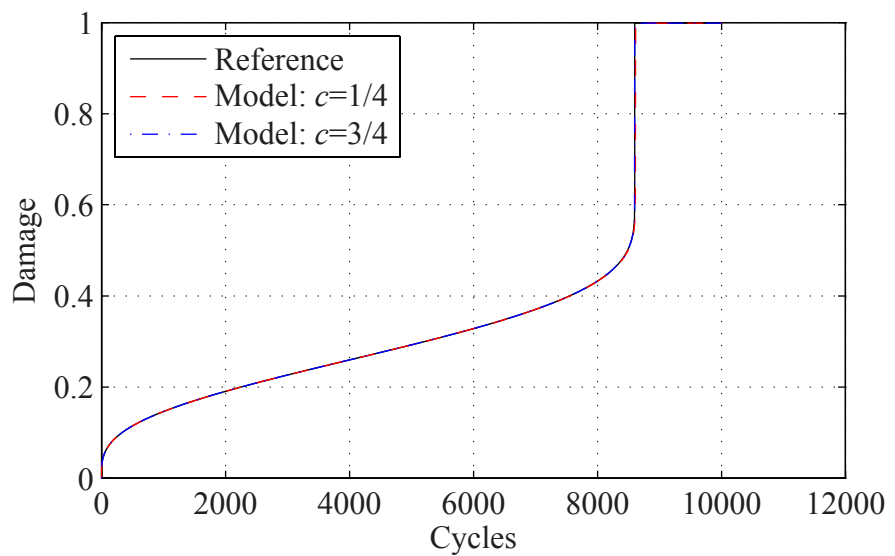


Figure 4: Nonlinear spring subjected to cyclic loading with maximum amplitude of 205 kPa.

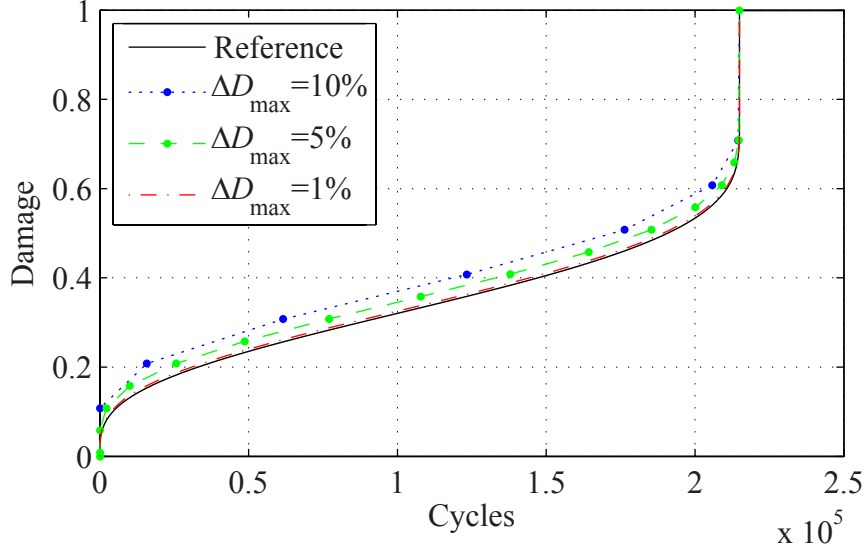


Figure 5: Performance of the adaptive time stepping algorithm with linear time stepping criterion.

is chosen based on the infinity norm:

$$\Delta t_i = \Delta D_{\max} / \|\mathbf{D}'(t_i)\|_\infty \quad (84)$$

in which, ΔD_{\max} is the error tolerance. In Fig. 5, the macrochronological time steps for the simulations with the tolerance values of $\Delta D_{\max} = 0.1$ and $\Delta D_{\max} = 0.05$ are indicated using the markers. The total number of resolved quasilinear microchronological cell evaluations are 10 and 17 for $\Delta D_{\max} = 0.1$ and $\Delta D_{\max} = 0.05$, respectively. When the tolerance is set to $\Delta D_{\max} = 0.01$, the damage evolution curve of the proposed multiscale algorithm is nearly indistinguishable from the reference simulation, but it required 76 quasilinear microchronological cell evaluations in contrast to the 214,932 nonlinear cycles resolved in the reference simulation. The proposed approach clearly indicates convergence to the reference solution as stricter tolerance is chosen.

Figure 6 shows the evolution of damage versus the number of loading cycles when a quadratic time stepping strategy is used. The simulations were performed by setting $\sigma_{\max} = 240\text{kPa}$ and $R\text{-ratio} = 0.1$. At time step, i , the time increment is chosen based on Eq. 54. For quadratic stepping, the macrochronological time step size is further restricted by the thermodynamic constraint (i.e., Eq. 60). Damage evolutions computed using three different error tolerance values (i.e., $\text{tol} = 8 \times 10^{-5}$, $\text{tol} = 1.6 \times 10^{-4}$ and $\text{tol} = 3.2 \times 10^{-4}$) are shown in Fig. 6. The simulations required 142, 102 and 71 quasilinear microchronological cell evaluations for increasingly tighter error tolerances, compared to the 2309 nonlinear resolved load cycles in the reference simulations. The case where $\text{tol} = 8 \times 10^{-5}$ is nearly

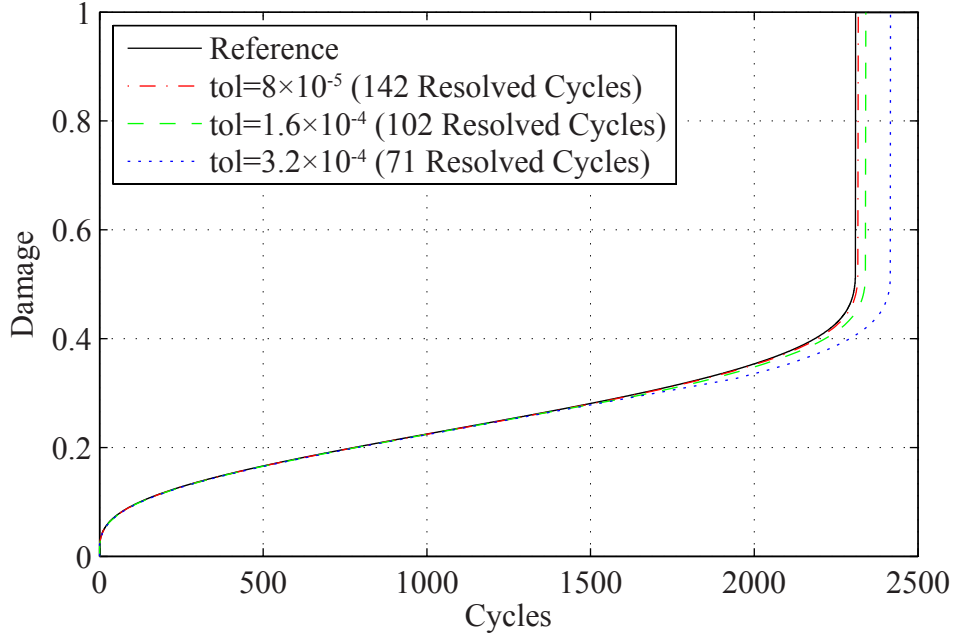


Figure 6: Performance of the adaptive time stepping algorithm with linear time stepping criterion.

indistinguishable from the reference simulation.

The next set of simulations was conducted under a more complex loading condition, in which two cyclic loads with different frequencies are applied simultaneously. The slow and fast components of the applied loading are of the following forms:

$$T_0(t) = \frac{\sigma_{\max} + \sigma_{\min}}{2} + \frac{\sigma_{\max} - \sigma_{\min}}{10} \sin\left(\frac{2\pi t}{d}\right) \quad (85)$$

$$T_1(\tau) = \frac{\sigma_{\max} - \sigma_{\min}}{2} \sin(2\pi\tau) \quad (86)$$

in which, the loading parameter, d , indicates the ratio between the fast and slow load frequencies. For instance, $d = 1000$ means the slow load undergoes one oscillation for every 1000 fast load oscillations. The amplitude of the slow load was set at 20% of the fast load amplitude. In contrast to the previous simulations, $T_0(t)$ is no longer constant and varies as a function of the macrochronological time, t .

Figures 7 and 8 show the evolution of damage as a function of the number of loading cycles when for $d = 1000$ and $d = 100$, respectively. The simulations were performed by setting $\sigma_{\max} = 265\text{kPa}$ and R-ratio = 0.1. $d = 1000$ case and $\sigma_{\max} = 265\text{kPa}$, R-ratio = 0.1 for the $d = 100$ case. The loading parameters are chosen to ensure that the two load cases lead to the same cycles to failure (9189 for both $d = 1000$ and $d = 100$). The linear time stepping criterion is employed in all the simulations. The effect of the slow loading

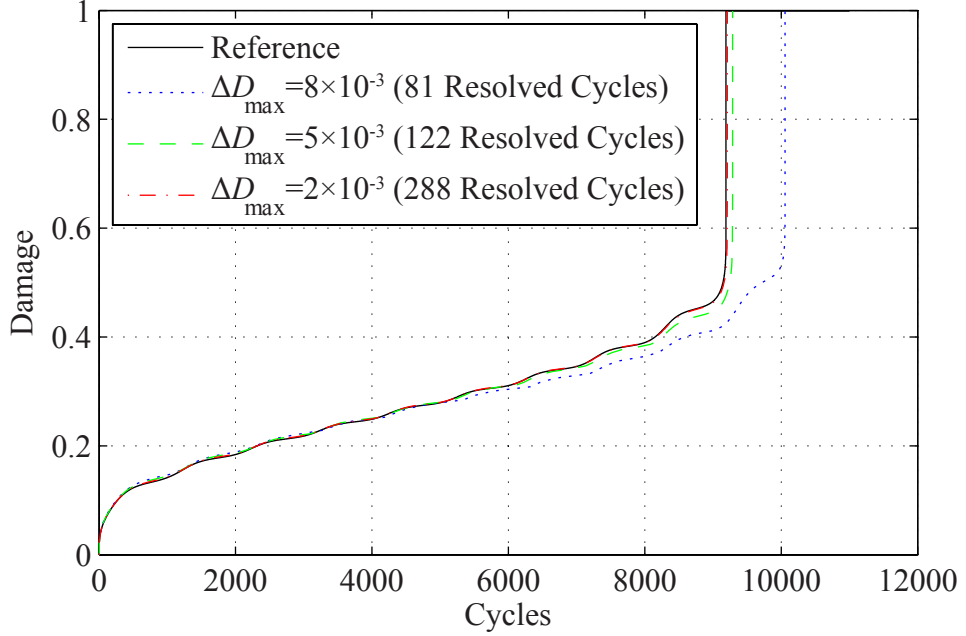


Figure 7: Performance of the multiscale model under superimposed cyclic loads ($d = 1000$).

component is observed in the damage curves as oscillations. Excellent accuracy is achieved when $\Delta D_{\max} = 2 \times 10^{-3}$ for the $d = 1000$ case, and when $\Delta D_{\max} = 2 \times 10^{-4}$ for $d = 100$ case, which corresponds to 288 and 2677 resolved quasilinear microchronological cell evaluations, respectively. The requirement of higher resolution in $d = 100$ case compared to the $d = 1000$ case, despite similar cycles-to-failure, is linked to the definition of the scaling parameter. In the case of two superimposed cyclic loads, the scaling parameter is no longer defined by the ratio between the life of the structure and the microchronological cell size, but rather the ratio between the slow and fast load frequencies (i.e., $\eta \sim 1/d$). The time stepping tolerance is therefore required to be an order of magnitude smaller for the $d = 100$, case in which, the scale separation is an order of magnitude less.

6.2 Multi-dimensional composite damage model

The performance of the proposed multiple time scale approach with the accelerated time integration strategy is further assessed in the context of the response of three-dimensional composite specimens. The failure response of the composite material is modeled based on the symmetric eigendeformation-based homogenization method (SEHM) [11]. The basis of SEHM is the mathematical homogenization theory with multiple spatial scales and the transformation field theory [14]. The details of this failure modeling approach and its implementation are presented in Refs. [11, 12]. A brief overview of the model is included herein. In the SEHM method, the response at the scale of the material microstructure (i.e., representative

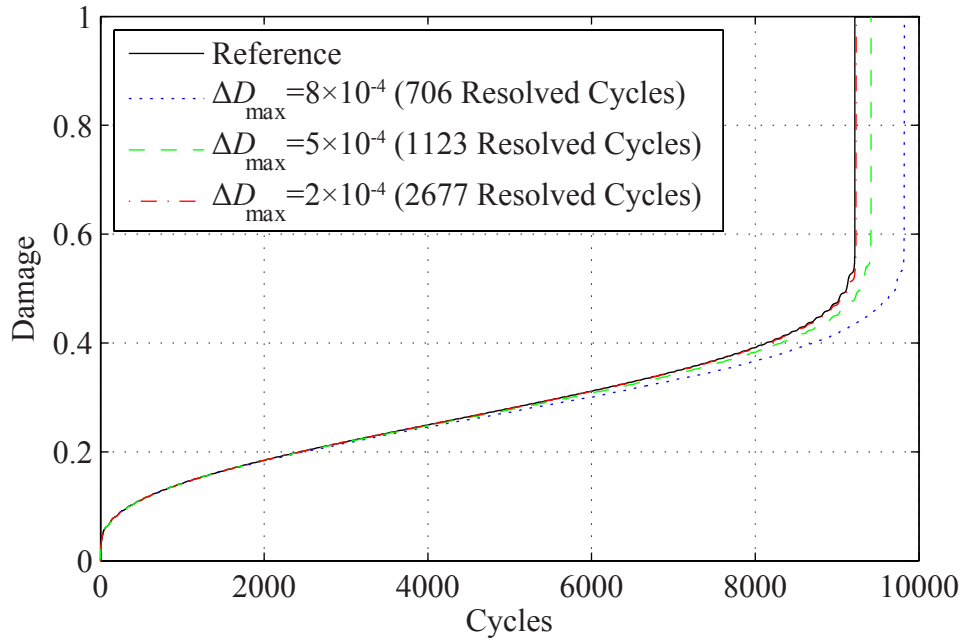


Figure 8: Performance of the multiscale model under superimposed cyclic loads ($d = 100$).

volume) is evaluated numerically based on the idea of precomputing certain microstructure information such as localization operators, concentration tensors and influence functions using linear elastic microstructure simulations, prior to a macroscale simulation. The inelastic response fields, such as damage tensors, are expressed using coarse basis functions, specified within subdomains (i.e., parts) of the representative volume as piecewise constant functions. Each part within the representative volume corresponds to a specific microstructural failure mode. The evaluation of the microstructural response fields are conducted within the reduced basis, leading to an orders of magnitude increase in computational efficiency compared to the standard spatial computational homogenization methods.

The equilibrium, kinematic, and boundary conditions for the SEHM composite model are provided in Eqs. 1-4. The composite material is taken to be a unidirectionally-reinforced polymer composite subjected to cyclic loads in the tension direction. The primary modes of failure at the scale of the microstructure are therefore fiber failure, delamination, and transverse matrix cracking. Using the SEHM method, the parts that correspond to the microstructure failure modes (illustrated in Fig. 9) are precomputed based on the nonlinear microscale simulations. The damage state within the microstructure is represented using four damage variables that are spatially piecewise constant within the associated microstructural subdomain (i.e., $\mathbf{D}^\eta = \{D_1^\eta, D_2^\eta, D_3^\eta, D_4^\eta\}$). The first three damage variables idealize the progressive failure of the fiber, transverse matrix cracking, and delamination, respectively. The fourth damage variable represents the interaction between the transverse matrix cracking

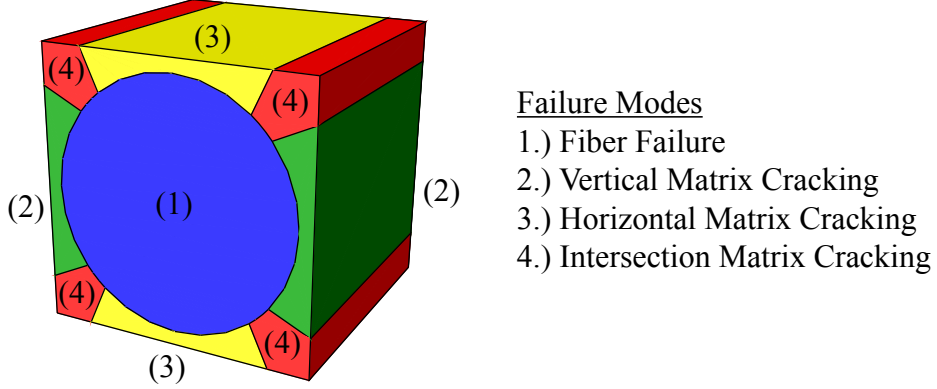


Figure 9: CFRP unit cell.

and delamination.

The constitutive relationship between the macroscopic stress, σ^η , and the macroscopic strain, ϵ^η , is expressed in terms of the damage variables as:

$$\sigma^\eta(\mathbf{x}, t) = \sum_{a=1}^4 (1 - D_a^\eta(\mathbf{x}, t)) \left(\mathbf{L}_a : \boldsymbol{\epsilon}^\eta(\mathbf{x}, t) + \sum_{b=1}^4 \mathbf{P}_{ab} : \boldsymbol{\mu}_b^\eta(\mathbf{x}, t) \right) \quad (87)$$

where $\boldsymbol{\mu}_b^\eta$ denotes the eigenstrain associated with part b , which is obtained through solving the nonlinear system of equations:

$$\sum_{b=1}^n (1 - D_b^\eta(\mathbf{x}, t)) \left(\mathbf{A}_{ab} : \boldsymbol{\epsilon}^\eta(\mathbf{x}, t) + \sum_{c=1}^n \mathbf{B}_{abc} : \boldsymbol{\mu}_c^\eta(\mathbf{x}, t) \right) = \mathbf{0} \quad a = 1, 2, 3, 4 \quad (88)$$

in which, \mathbf{L}_a , \mathbf{P}_{ab} , \mathbf{A}_{ab} , and \mathbf{B}_{abc} tensors are computed using the microstructural influence functions - numerical approximations to the fundamental solutions of the microstructure problems. These coefficient tensors provide the effect of the microscale morphology on the homogenized constitutive law (i.e., Eq. 87):

$$\mathbf{L}_a = \frac{1}{|\Theta|} \int_{\Theta_a} \mathbf{L}(\mathbf{y}) : (\mathbf{I} + \mathbf{G}(\mathbf{y})) d\mathbf{y} \quad (89)$$

$$\mathbf{P}_{ab} = \frac{1}{|\Theta|} \int_{\Theta_a} \mathbf{L}(\mathbf{y}) : \hat{\mathbf{P}}_b(\mathbf{y}) d\mathbf{y} \quad (90)$$

$$\mathbf{A}_{ab} = \int_{\Theta_b} \hat{\mathbf{P}}_a^\top(\mathbf{y}) : \mathbf{L}(\mathbf{y}) : (\mathbf{I} + \mathbf{G}(\mathbf{y})) d\mathbf{y} \quad (91)$$

$$\mathbf{B}_{abc} = \int_{\Theta_b} \hat{\mathbf{P}}_a^\top(\mathbf{y}) : \mathbf{L}(\mathbf{y}) : \hat{\mathbf{P}}_c(\mathbf{y}) d\mathbf{y} \quad (92)$$

Table 1: Material Properties

Matrix Properties (Isotropic)							
E [GPa]	ν	a	b	γ			
3.55	0.35	0.05	32.0	2.5			
Fiber Properties (Transverly Isotropic)							
E_1 [GPa]	E_2 [GPa]	G_{12} [GPa]	ν_{12}	ν_{23}	a	b	γ
263.00	13.00	27.50	0.32	0.20	0.05	340.0	50.0

$$\hat{\mathbf{P}}_a(\mathbf{y}) = \int_{\Theta_a} \mathbf{g}_{ph}(\mathbf{y}, \hat{\mathbf{y}}) d\hat{\mathbf{y}} \quad (93)$$

where Θ is the domain of the representative volume, and Θ_a is the domain of part a (Fig. 9). \mathbf{g}_{ph} and \mathbf{G} are the damage-induced and elastic polarization functions, respectively, computed as the symmetric gradients of the microstructural influence functions. superscript \top denotes the transpose operator.

The evolution of the damage variables are idealized using a form similar to Eq. 68:

$$g_a(\boldsymbol{\varepsilon}_a^\eta(t), D_a^\eta(t)) = \left[\frac{\Phi_a^\eta(t)}{D_a^\eta(t)} \right]^{\gamma_a} \langle \dot{\Phi}_a^\eta(t) \rangle_+ \quad (94)$$

where γ_a is a material parameter controlling the fatigue behavior of the corresponding constituent material that occupies part a , and $\boldsymbol{\varepsilon}_a^\eta(t)$ is the average strain within part a given by:

$$\boldsymbol{\epsilon}_a^\eta = \boldsymbol{\epsilon}_a(\mathbf{x}, t) = \mathbf{E}_a : \boldsymbol{\epsilon}^\eta(\mathbf{x}, t) + \sum_{b=1}^n \mathbf{F}_{ab} : \boldsymbol{\mu}_b^\eta(\mathbf{x}, t) \quad (95)$$

The coefficient tensors \mathbf{E}_a and \mathbf{F}_{ab} are computed with the following functions:

$$\mathbf{E}_a = \frac{1}{|\Theta|} \int_{\Theta_a} \mathbf{I} + \mathbf{G}(\mathbf{y}) d\mathbf{y} \quad (96)$$

$$\mathbf{F}_{ab} = \frac{1}{|\Theta|} \int_{\Theta_a} \hat{\mathbf{P}}_b(\mathbf{y}) d\mathbf{y} \quad (97)$$

The expression of the damage evolution function $\Phi_a^\eta(v_i^\eta(t))$ is taken to be identical to Eq. 69 as a function of the damage equivalent strain, which is now expressed as:

$$v_a^\eta = v_a(\boldsymbol{\varepsilon}_a^\eta(\mathbf{x}, t)) = \sqrt{\frac{1}{2} \boldsymbol{\varepsilon}_a^\eta : \mathbf{C}_a : \boldsymbol{\varepsilon}_a^\eta} \quad (98)$$

where \mathbf{C}_a is the elasticity tensor of the constituent material of part a .

The values of the material parameters for the fiber and the resin employed in the verification simulations described below are shown in Table 1. The fiber and the matrix parameters

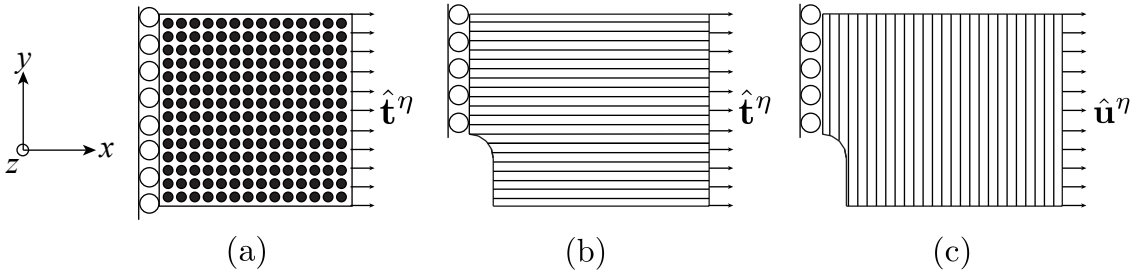


Figure 10: The geometry and fiber orientation used in the verification study: (a)specimen fibers oriented in the z-direction; (b) 0^0 composite specimen with a notch, and (c) 90^0 composite specimen with a notch.

employed reflect the parameters of a graphite reinforced epoxy composite. The fiber is taken to be insensitive to progressive fatigue damage accumulation by setting a high value for the fatigue parameter, γ_f . If a part resides in the subdomain of the microstructure that is occupied by the fiber or the resin, the material parameters of the part is set to the pertinent material parameters.

The performance of the proposed accelerated multiple-time scale model is assessed using three sets of verification tests. The geometry and loading of the numerical specimens employed in these three tests are illustrated in Fig. 10. All simulations are conducted in 3-D. In the first set of simulations, a uniform composite specimen was subjected to uniaxial sinusoidal traction. The fibers are oriented along the z-direction as shown in Fig. 10a. The R -ratio of the loading is set to 0.1. A single hexahedral finite element is employed to represent the macrostructure of the composite in both the reference and the multiple time scale simulations. The adaptive step size criteria was set to $\Delta D_{\max} = 0.01$. Figure 11 shows the progressive evolution of damage variables within the matrix (i.e., D_2 , D_3 , and D_4) as a function of loading cycles. The macrochronological time steps in which a microchronological cell is resolved in the proposed multiscale model are indicated using markers in Fig. 11. The cyclic failure accumulation predicted by the cycle-by-cycle nonlinear reference simulations and the multiscale model show that the transverse matrix damage accumulation (indicated by increasing damage in D_2) occurs faster than delamination. The onset of the ultimate failure is due to the transverse matrix cracking. The proposed multiscale model is in excellent agreement with the reference model. The computational cost of the multiscale model is 38 quasilinear macrochronological cell evaluations compared to 882 nonlinear, inelastic cycles resolved in the reference simulation.

A second set of simulations was performed to assess the capability of the multiscale model in capturing the damage initiation behavior in the notched specimens. The geometry of the specimen is shown in Fig. 10b. The fibers are oriented parallel to the applied cyclic loading.

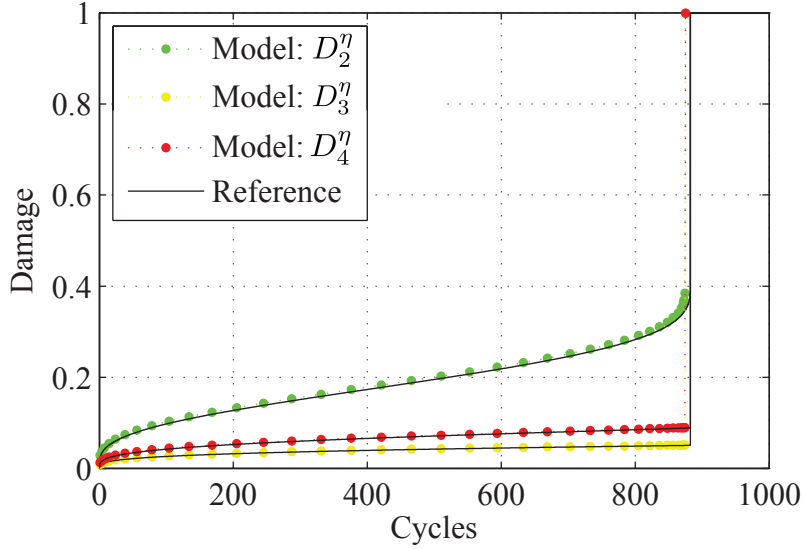


Figure 11: Single square element numerical verification for the CFRP constitutive law.

The adaptive step size criteria was set to $\Delta D_{\max} = 0.005$. Figure 12 compares the damage contours around the notch computed by the reference simulation that evaluates the fully resolved governing equations for every cycle and the fast temporal homogenization method. The contours display the matrix damage after 474 loading cycles, 1982 loading cycles, and at the onset of crack formation. The onset of crack formation is predicted at 3066 load cycles by the reference simulation and 3060 load cycles by the proposed multiscale model. The damage state around the notch tip throughout the course of the simulation, and the time to failure initiation are predicted with very reasonable accuracy (< 0.2% error computed in terms of load cycles to initiation). The computational cost of the multiscale model is 113 quasilinear macrochronological cell evaluations compared to 3066 nonlinear, inelastic cycles resolved in the reference simulation. In real CPU time, the proposed model predicted the failure initiation approximately 30 times faster than the reference simulation.

A third set of simulations was performed to assess the capability of the multiscale model in capturing the damage propagation behavior in the notched specimens. The third test was conducted with the fibers oriented perpendicular to the applied sinusoidal displacement as in Fig. 10c. The adaptive step size criteria was set to $\Delta D_{\max} = 0.005$. A slightly increased macrochronological tolerance is employed to maintain high accuracy during the damage propagation phase. Figure 13 compares the matrix damage contours and the crack propagation around the notch computed by the reference simulation that evaluates the fully resolved governing equations for every cycle and the fast temporal homogenization method. The contours display the matrix damage at the onset of crack initiation, after 750 cycles, and 1000 cycles. The onset of crack initiation was predicted as 609 load cycles by the reference

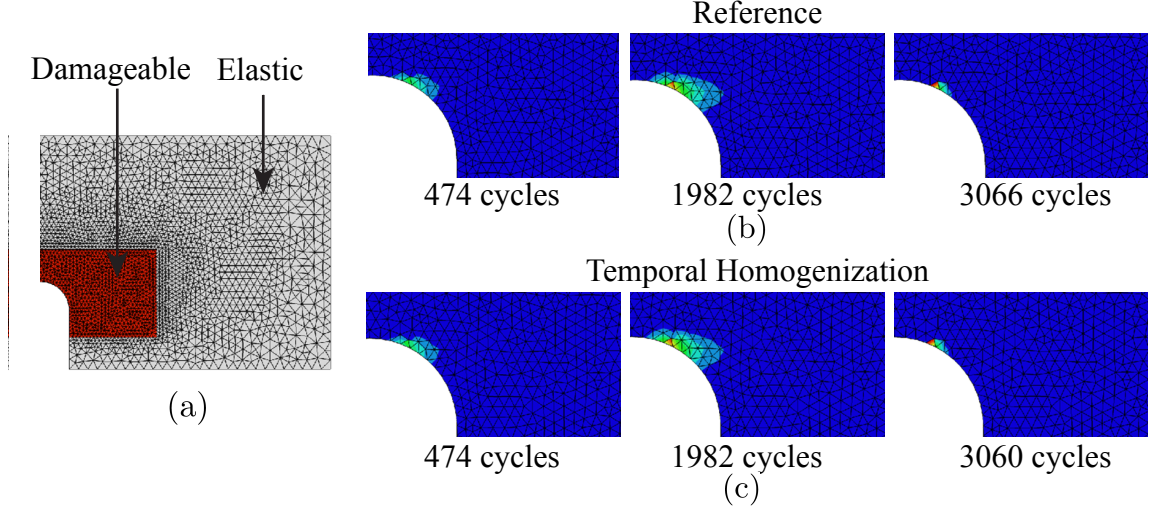


Figure 12: Numerical verification for a 0° notched specimen: (a) mesh with inelastic damage zone in red, (b) damage contours for the reference simulation (c) damage contours for the multitemporal simulation.

simulation and 631 load cycles by the proposed multiscale model. Figure 13 indicates a close match between the reference and the multiscale models throughout the crack incubation and propagation periods. Figure 14 shows the evolution of the crack length as a function of the number of applied load cycles. Despite the slightly faster crack growth predicted by the multiscale model, the rapid growth after initiation and progressive slow-down of the crack growth rate are accurately captured. The reduction of the crack growth rate is due to the displacement controlled loading. As the crack grows, the specimen becomes more compliant and needs a smaller applied stress to achieve the required displacement subsequently reducing the stress at the critical damage zone and retarding the crack growth.

7 Conclusions

A fast temporal homogenization methodology for modeling and prediction of failure in materials and material systems undergoing fatigue loading conditions was described in this manuscript. The time integrator achieves high computational efficiency in solving fatigue problems due to the explicit nature of the algorithm, requiring no nonlinear iterations during time stepping. Adaptive time stepping metrics were proposed that achieve high computational performance while maintaining accuracy in fatigue life predictions. A thermodynamic analysis showed the method satisfies the dissipative inequality for a wide class of continuum damage approaches. The method helps achieve the high degree of computational performance critical to the prediction of life and failure in large-scale structures and presents a

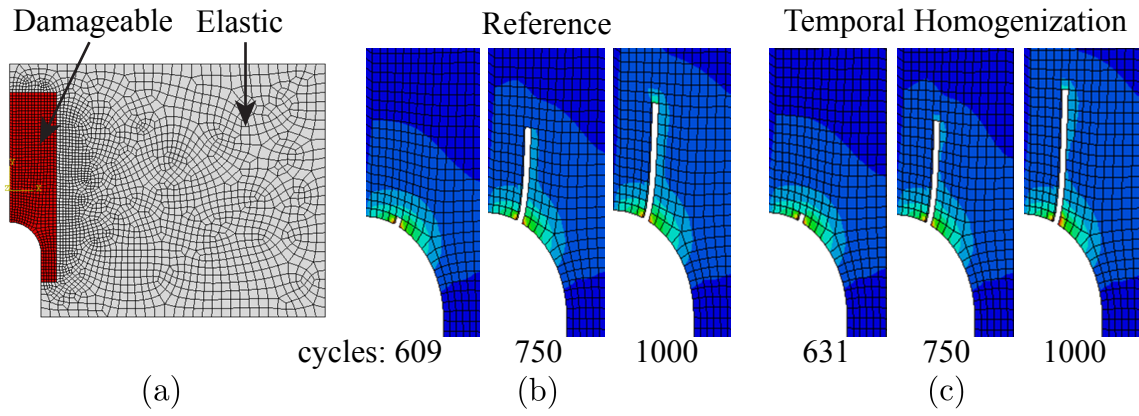


Figure 13: Numerical verification for a 90° notched specimen: (a) mesh with inelastic damage zone in red, (b) damage contours for the reference simulation (c) damage contours for the multitemporal simulation.

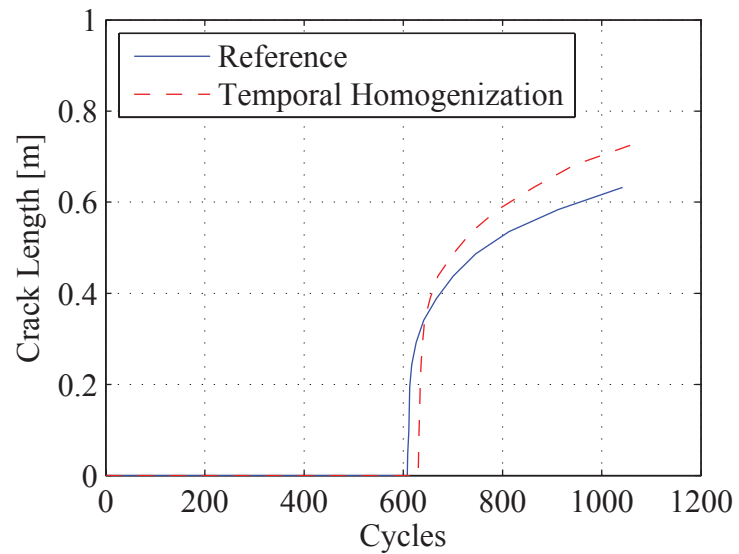


Figure 14: Crack length versus loading cycles for the 90° notched specimen verification.

path forward in tackling the difficult problem of life prediction in brittle materials. Despite good accuracy during numerical verifications, a more detailed experimental analysis will provide validation of the fast temporal scale homogenization. For this purpose, a detailed experimental investigation of fatigue in the carbon fiber reinforced polymer, IM7/977-3, will be undertaken in the near future.

8 Acknowledgements

The authors gratefully acknowledge the financial support provided by the Aerospace Systems Directorate of the Air Force Research Laboratory (Contract No: GS04T09DBC0017 through High Performance Technologies Inc.).

References

- [1] R. Abu Al-Rub and G. Voyatzis. A finite strain plastic-damage model for high velocity impact using combined viscosity and gradient localization limiters: Part I theoretical formulation. *Int. J. Damage Mech.*, 15:293–334, 2006.
- [2] A. Acharya and A. Sawant. On a computational approach for the approximate dynamics of average variables in nonlinear ode systems: toward the derivation of constitutive laws of the rate type. *J. Mech. Phys. Solids*, 54:2183–2213, 2006.
- [3] I. Babuska. Homogenization and application. mathematical and computational problems. In B. Hubbard, editor, *Numerical Solution of Partial Differential Equations - III, SYNSPADE*. Academic Press, 1975.
- [4] A. Benssousan, J. Lions, and G. Papanicolaou. *Asymptotic Analysis for Periodic Structures*. North-Holland, Amsterdam, 1978.
- [5] E. Benvenuti, G. Borino, and A. Tralli. A thermodynamically consistent nonlocal formulation for damaging materials. *Eur. J. Mech. A-Solid.*, 21:535–553, 2002.
- [6] M. Borden, C. Verhoosel, M. Scott, T. Hughes, and C. Landis. A phase-field description of dynamic brittle fracture. *Comput. Method. Appl. M.*, 217-220:77–95, 2012.
- [7] J. Chaboche. Continuum damage mechanics: Part I general concepts. *J. Appl. Mech.*, 55:59–64, 1988.
- [8] P. Chakraborty and S. Ghosh. Accelerating cyclic plasticity simulations using an adaptive wavelet transformation based multitime scaling method. *Int. J. Numer. Meth. Eng.*, 93:1425–1454, 2013.

- [9] C. L. Chow and Y. Wei. A model of continuum damage mechanics for fatigue failure. *Int. J. Fatigue*, 50:301–306, 1991.
- [10] E. Coenen, V. Kouznetsova, and M. Geers. Novel boundary conditions for strain localization analyses in microstructural volume elements. *Int. J. Numer. Meth. Eng.*, 90: 1–21, 2012.
- [11] R. Crouch and C. Oskay. Symmetric mesomechanical model for failure analysis of heterogeneous materials. *Int. J. Multiscale Com.*, 8:447–461, 2010. ISSN 1543-1649.
- [12] R. Crouch and C. Oskay. Multiple spatio-temporal scale modeling of composites subjected to cyclic loading. *Comput. Mech.*, 51:93–107, 2013.
- [13] R. Crouch and C. Oskay. Experimental and computational investigation of progressive damage accumulation in CFRP composites. *Compos. Part B-Eng.*, 48:59–67, 2013.
- [14] G. J. Dvorak. Transformation field analysis of inelastic composite materials. *P. Roy. Soc. A-Math. Phy.*, 437:311–327, 1992.
- [15] Y. Efendiev and T. Y. Hou. *Multiscale Finite Element Methods*. Springer, 2009.
- [16] F. Feyel and J. Chaboche. FE2 multiscale approach for modelling the elastoviscoplastic behavior of long fiber sic/ti composite materials. *Comput. Method. Appl. M.*, 183:309–330, 2000.
- [17] J. Fish and Q. Yu. Computational mechanics of fatigue and life predictions for composite materials and structures. *Comput. Method. Appl. M.*, 191:4827–4849, 2002.
- [18] J. Fish, M. Bailakanavar, L. Powers, and T. Cook. Multiscale fatigue life prediction model for heterogeneous materials. *Int. J. Numer. Meth. Eng.*, 91:1087–1104, 2012.
- [19] J. Guedes and N. Kikuchi. Preprocessing and postprocessing for materials based on the homogenization method with adaptive finite element methods. *Comput. Method. Appl. M.*, 83:143–198, 1990.
- [20] M. Gurtin, E. Fried, and L. Anand. *The Mechanics and Thermodynamics of Continua*. Cambridge University Press, 2013.
- [21] T. J. R. Hughes. Multiscale phenomena: Greens functions, the dirichlet-to-neumann formulation, subgrid scale models, bubbles and the origins of stabilized methods. *Comput. Method. Appl. M.*, 127:387–401, 1995.

- [22] D. Joseph, P. Chakraborty, and S. Ghosh. Wavelet transformation based multi-level scaling for crystal plasticity FE simulations under cyclic loading. *Comput. Method. Appl. M.*, 199:2177–2194, 2010.
- [23] D. Krajcinovic. *Damage Mechanics*, volume 41 of *North Holland Series in Applied Mathematics and Mechanics*. Elsevier Science, 1996.
- [24] D. Krajcinovic and G. U. Fonseca. The continuous damage theory of brittle materials part 1: General theory. *J. Appl. Mech.*, 48:809–815, 1981.
- [25] T. Liebe, P. Steinmann, and A. Benallal. Theoretical and computational aspects of a thermodynamically consistent framework for geometrically linear gradient damage. *Comput. Method. Appl. M.*, 190:6555–6576, 2001.
- [26] P. Maimi, P. Camanhob, J. Mayugoa, and C Davila. A continuum damage model for composite laminates: Part I constitutive model. *Mech. Mater.*, 39:897–908, 2007.
- [27] S. Mesarovic and J. Padbidri. Minimal kinematic boundary conditions for simulations of disordered microstructures. *Philos. Mag.*, 85:65–78, 2005.
- [28] C. Oskay. Variational multiscale enrichment for modeling coupled mechano-diffusion problems. *Int. J. Numer. Meth. Eng.*, 89:686–705, 2012.
- [29] C. Oskay and J. Fish. Fatigue life prediction using 2-scale temporal asymptotic homogenization. *Int. J. Numer. Meth. Eng.*, 61:329–359, 2004.
- [30] C. Oskay and J. Fish. Multiscale modeling of fatigue for ductile materials. *Int. J. Multiscale Com.*, 2, 2004.
- [31] C. Oskay and J. Fish. Eigendeformation-based reduced order homogenization for failure analysis of heterogeneous materials. *Comput. Method. Appl. M.*, 196:1216–1243, 2007.
- [32] M. Paas, P. Schreurs, and W. Brekelmans. A continuum approach to brittle and fatigue damage: Theory and numerical procedures. *Int. J. Solids. Struct.*, 30:579–599, 1993.
- [33] C. Polizzotto. Unified thermodynamic framework for nonlocal/gradient continuum theories. *Eur. J. Mech. A-Solid.*, 22:651–668, 2003.
- [34] P. Rosakis, A. Rosakis, G. Ravichandran, and J. Hodowany. A thermodynamic internal variable model for the partition of plastic work into heat and stored energy in metals. *J. Mech. Phys. Solids*, 48:581–607, 2000.
- [35] J. C. Simo and J. W. Ju. Strain and stress based continuum damage models I formulation. *Int. J. Solids Struct.*, 23(7):821–840, 1987.

- [36] M. Slemrod and A. Acharya. Time-averaged coarse variables for multi-scale dynamics. *Q. Appl. Math.*, 70:793–803, 2012.
- [37] K. Terada and N. Kikuchi. Nonlinear homogenization method for practical applications. In S. Ghosh and M. Ostoja-Starzewski, editors, *Computational Methods in Micromechanics*, volume AMD-212/MD-62, pages 1–16. ASME, 1995.
- [38] J. Vree, W. Brekelmans, and M. Gils. Comparison of nonlocal approaches in continuum damage mechanics. *Comput. Struct.*, 55:581–588, 1995.